Astronomy & Astrophysics manuscript no. Paper_final
March 2, 2022

Letter to the Editor

A major asymmetric ice trap in a planet-forming disk: I. Formaldehyde and methanol

Nienke van der Marel[1,2], Alice S. Booth[3], Margot Leemker[3], Ewine F. van Dishoeck[3,4], and Satoshi Ohashi[5]

[1] Physics & Astronomy Department, University of Victoria, 3800 Finnerty Road, Victoria, BC, V8P 5C2, Canada
[2] Banting Research fellow
[3] Leiden Observatory, Leiden University, 2300 RA Leiden, the Netherlands
[4] Max-Plank-Institut fur Extraterrestrische Physik, Giessenbachstraße 1, D-85748 Garching, Germany
[5] RIKEN Cluster for Pioneering Research, 2-1, Hirosawa, Wako-shi, Saitama 351-0198, Japan

Received April, 2021; accepted June, 2021

ABSTRACT

Context. The chemistry of planet-forming disks sets the exoplanet atmosphere composition and the prebiotic molecular content. Dust traps are of particular importance as pebble growth and transport are crucial for setting the chemistry where giant planets are forming.
Aims. The asymmetric Oph IRS 48 dust trap located at 60 au radius provides a unique laboratory for studying chemistry in pebble-concentrated environments in warm Herbig disks with low gas-to-dust ratios down to 0.01.
Methods. We use deep ALMA Band 7 line observations to search the IRS 48 disk for H_2CO and CH_3OH line emission, the first steps of complex organic chemistry.
Results. We report the detection of 7 H_2CO and 6 CH_3OH lines with energy levels between 17 and 260 K. The line emission shows a crescent morphology, similar to the dust continuum, suggesting that the icy pebbles play an important role in the delivery of these molecules. Rotational diagrams and line ratios indicate that both molecules originate from warm molecular regions in the disk with temperatures >100 K and column densities $\sim 10^{14}$ cm^{-2} or a fractional abundance of $\sim 10^{-8}$ and with H_2CO/CH_3OH~0.2, indicative of ice chemistry. Based on arguments from a physical-chemical model with low gas-to-dust ratios, we propose a scenario where the dust trap provides a huge icy grain reservoir in the disk midplane or an 'ice trap', which can result in high gas-phase abundances of warm COMs through efficient vertical mixing.
Conclusions. This is the first time that complex organic molecules have been clearly linked to the presence of a dust trap. These results demonstrate the importance of including dust evolution and vertical transport in chemical disk models, as icy dust concentrations provide important reservoirs for complex organic chemistry in disks.

Key words. Astrochemistry – Protoplanetary disks

1. Introduction

Protoplanetary disks around young stars are the birth cradles of planets, and the chemical composition in these disks sets the exoplanet atmospheric composition and the formation of prebiotic molecules on their surfaces (Ehrenfreund & Charnley 2000; Öberg & Bergin 2021). So far, mostly simple molecules have been detected in disks (e.g. Dutrey et al. 1997; Thi et al. 2004; Öberg et al. 2010, 2015; Walsh et al. 2016), and their abundances are set by photodissociation in the surface layers and freeze-out in the midplane (Bergin et al. 2007). Complex organic molecules (COMs) may be present but are expected to be mostly locked up in ices. CO ice chemistry is crucial for the formation of complex organic molecules which can be thermally released into the gas-phase (Herbst & van Dishoeck 2009). For Herbig disks, COMs cannot form in situ since they are warm and lack a large CO-ice reservoir (Agúndez et al. 2018). Surprisingly, CH_3OH was recently detected in the Herbig disk HD100546 (Booth et al. 2021). This detection can be understood when CH_3OH ice is inherited from earlier stages, followed by radial transport and sublimation at its iceline. Pebble growth and transport are known to play an important role in the chemical composition of disks and resulting exoplanet atmospheres (Cridland et al. 2017; Krijt et al. 2020). The connection between pebbles and ice chemistry can be studied directly in so-called dust traps (concentrations of dust grains), possibly revealing a much richer chemistry as dust rings are colder in the midplane (Alarcón et al. 2020) while exposed dust cavity walls can reveal sublimated midplane products (Cleeves et al. 2011; Mulders et al. 2011).

Dust traps are thought to be the main explanation for the observed narrow dust rings and asymmetries in high-resolution ALMA observations revealing also a segregation between gas and dust (e.g. van der Marel et al. 2013; Pérez et al. 2014; Andrews et al. 2018). Pressure bumps at gap edges trap larger dust grains due to drag forces between gas and dust (Weidenschilling 1977), which can explain the appearance of dust rings in protoplanetary disks as the dust is prevented from drifting inwards (Pinilla et al. 2012a). In some cases, the pressure bump can become susceptible to the Rossby Wave Instability and form long-lived vortices (Barge & Sommeria 1995), which trap the dust in the azimuthal direction. The Herbig disk Oph IRS 48 is a textbook example of such a dust trap showing an asymmetric dust concentration south of the star (van der Marel et al. 2013, 2015), and thus an ideal target for studying complex organic chemistry in a pebble-concentrated environment.

The presence of warm H_2CO in the IRS 48 disk was discovered by van der Marel et al. (2014). H_2CO is a precursor of more complex organic molecules such as CH_3OH through CO ice hy-

Table 1. Detected molecular lines, line properties and disk integrated fluxes

Molecule	Transition	Rest frequency (GHz)	E_u (K)	g_u	log A_{ul}	F_{int} (mJy km s^{-1})
o-H_2CO	$5_{1,5}$-$4_{1,4}$	351.768648	62	33	-2.92013	836
o-H_2CO	$5_{3,3}$-$4_{3,2}$	364.275141	158	33	-3.05097	391
o-H_2CO	$5_{3,2}$-$4_{3,1}$	364.288914	158	33	-3.05065	574
p-H_2CO	$5_{0,5}$-$4_{0,4}$	362.736024	52	11	-2.86264	577
p-H_2CO	$5_{2,4}$-$4_{2,3}$	363.945876	100	11	-2.93377	377
p-H_2CO	$5_{4,2}$-$4_{4,1}$/$5_{4,1}$-$4_{4,0}$[a]	364.103257	241	11	-3.30139	99
a-CH_3OH	$14_{1,13}$-$14_{0,14}$	349.106997	260	116	-3.35603	198
a-CH_3OH	$1_{1,1}$-$0_{0,0}$	350.905100	17	12	-3.47949	89
e-CH_3OH	$4_{0,4}$-$3_{-1,3}$	350.687651	36	36	-4.06195	215
e-CH_3OH	$7_{-2,6}$-$6_{-1,5}$	363.739868	87	60	-3.76767	141
e-CH_3OH	$8_{1,7}$-$7_{2,5}$	361.852195	105	68	-4.11248	125
e-CH_3OH	$11_{0,11}$-$10_{1,9}$	360.848946	166	92	-3.91831	155

[a] Lines are blended.
Rest frequencies and other properties are taken from CDMS: E_u is the upper energy level, g_u the degeneracy and A_{ul} the Einstein A-coefficient.

drogenation (e.g. Watanabe & Kouchi 2002; Fuchs et al. 2009). The morphology appeared to be cospatial with the dust crescent, but the detection was tentative. CH_3OH was not detected in this work, but upper limits were derived. The H_2CO/CH_3OH abundance ratio can be used as tracer for the formation mechanism (Garrod et al. 2006), since CH_3OH can only be formed efficiently through ice chemistry, whereas H_2CO has both an ice- and gas-phase route (e.g. Walsh et al. 2014). Gas-phase dominated H_2CO formation implies a ratio>1 and ice-phase a ratio<1. However, the derived H_2CO/CH_3OH ratio from van der Marel et al. (2014) of $\gtrsim$0.3 was inconclusive about the formation mechanism.

Whereas H_2CO has been routinely detected in a range of protoplanetary disks (e.g. Pegues et al. 2020), CH_3OH has only been detected in the TW Hya disk (Walsh et al. 2016), the young IRAS04302 disk (Podio et al. 2020) and outburst disk V883 Ori (van 't Hoff et al. 2018; Lee et al. 2019) and recently in the Herbig disk HD100546 (Booth et al. 2021).

In this work, we present the detection of multiple CH_3OH and H_2CO transitions in the IRS 48 system, only the second Herbig disk with observed COMs and the first disk where the COM production can be linked directly to the dust trap.

2. Observations

Oph IRS 48 is an A0 star located in the Ophiuchus cloud at a distance of 135 pc (Gaia Collaboration et al. 2018). This disk, inclined at 50°, shows an asymmetric millimeter-dust concentration at 60 au, in contrast with a full ring in gas and small dust grains (van der Marel et al. 2013) and has an estimated gas disk mass of only 0.6 $M_{\rm Jup}$ (van der Marel et al. 2016). IRS 48 has been observed using the Atacama Large Millimeter/submillimeter Array (ALMA) in Band 7 in polarization mode in Cycle 5 in August 2018 (2017.1.00834.S, PI:Adriana Pohl). The continuum polarization data are presented by Ohashi et al. (2020), and the main calibration and reduction process is described in detail in that work. The total on-source integration time is 89 minutes. The continuum is subtracted in the uv-plane using the CASA task `uvcontsub` with a first order polynomial. The spectral setup contains four spectral windows at 349.7, 351.5, 361.6 and 363.5 GHz, with a bandwidth of 1875 GHz in each window and a channel width of 1953 kHz or ~1.6 km s^{-1}.

Seven H_2CO and six CH_3OH transitions were identified using the matched-filter-technique (Loomis et al. 2018), listed in Table 1, for E_u levels between 17 and 260 K. H_2CO transitions are identified as ortho (o-) and para (p-) transitions, respectively. Each line was imaged using the `tclean` task at the channel resolution, using natural weighting. The final channel cubes have a beam size of 0.63×0.50" and a rms noise of $\sigma_{\rm rms}$ ~1.2 mJy beam^{-1} channel^{-1}. The brightest lines (H_2CO $5_{0,5}$ − $4_{0,4}$ and CH_3OH $4_{0,4}$ − $3_{1,3}$) are also imaged using Briggs weighting with a robust of 0.5 for a resolution of 0.55×0.44".

Spectra are extracted from the naturally weighted cubes using Keplerian masking (using d=135 pc, i=50° and M_*=2.0 $M_\odot$) and presented in Figure A.1. All cubes show a clear Keplerian pattern along the southern part of the disk. Some lines are located adjacent to other lines, i.e. the H_2CO $5_{3,3}$-$4_{3,2}$ and $5_{3,2}$-$4_{3,1}$ transitions, so their line wings overlap in 2 channels.

The disk-integrated spectra are resolved even at our low spectral resolution, ranging from -2 to 12 km s^{-1} with $v_{\rm source}$=4.55 km s^{-1}. The CH_3OH lines appear to have somewhat more prominent line wings (corresponding to an inner 30 au radius) than the H_2CO lines. The spectra are integrated over the entire individual profiles (avoiding overlap with adjacent features) and the disk integrated fluxes are reported in Table 1. The H_2CO $5_{4,2}$-$4_{4,1}$ and $5_{4,1}$-$4_{4,0}$ fluxes are computed by dividing their shared flux by 2. The integrated fluxes are detected with a range between 5 and 42$\sigma_{\rm int}$, with $\sigma_{\rm int}$ ~20 mJy km s^{-1}, whereas the calibration uncertainty is 10%.

Zero-moment maps are created using Keplerian masking and presented in Figure A.2. The central position is set at J2000 16h27m37.180s, -24°30'35.48", based on Gaia DR2 (Gaia Collaboration et al. 2018). Spectra and moment maps of the two brightest lines are presented in Figure 1.

3. Results

Both H_2CO and CH_3OH lines are firmly detected. IRS 48 is the second known Herbig disk with a detection of CH_3OH, following HD 100546 (Booth et al. 2021). It is immediately clear that both molecules follow the dust trap morphology (Figure 1), in contrast with ^{13}CO which shows a full disk ring, just like the small grains (van der Marel et al. 2013). This confirms the find-

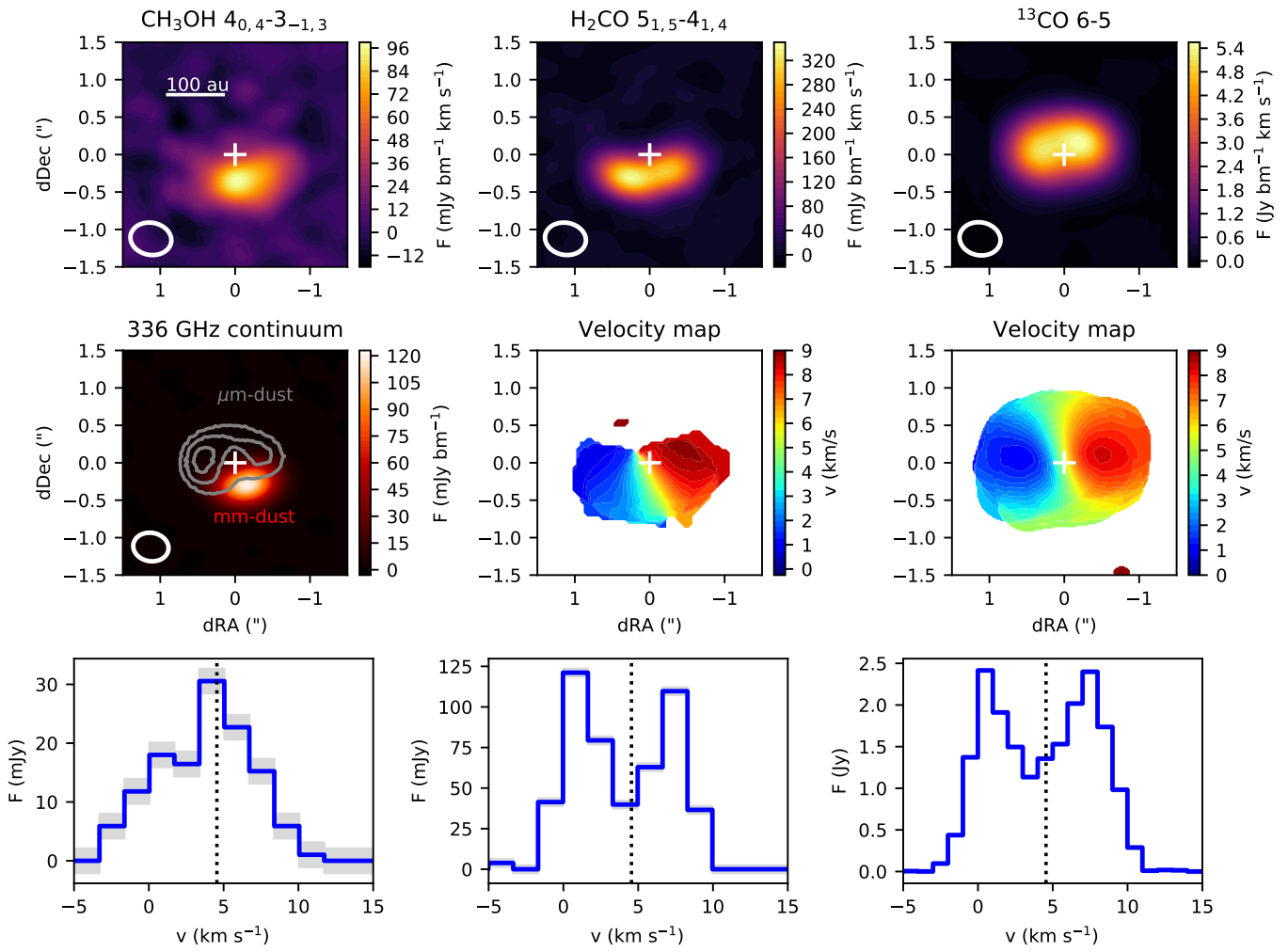

Fig. 1. Overview of the brightest H_2CO and CH_3OH lines using Briggs weighting, the 336 GHz continuum and the ^{13}CO 6-5 map with a similar beam size for comparison. The top row shows the zero-moment maps, the middle row the continuum and the first moment maps and the bottom row the disk integrated spectra. The μm-sized grain distribution as traced by 19 μm VISIR data (Geers et al. 2007) is indicated in the continuum image. The source velocity is indicated by a vertical dotted line. The grey shades indicate the noise levels in the spectra.

ings of van der Marel et al. (2014) of their suggested location of the H_2CO emission.

Figure 1 presents the data for the two brightest line transitions: the H_2CO $5_{1,5} - 4_{1,4}$ and the CH_3OH $4_{0,4} - 3_{0,3}$ lines. The maps are compared with the 355 GHz continuum from the same dataset and with the ^{13}CO 6–5 intensity maps. The ^{13}CO data are taken from van der Marel et al. (2016) and imaged using uv-tapering for a similar beam size as the Band 7 data presented here. The first-moment maps of the H_2CO and CH_3OH emission are consistent with Keplerian motion along the southern half of the disk.

A comparison between the images in both the radial and azimuthal directions is presented in Figure 2. The profiles are extracted by deprojecting the zero-moment maps assuming a position angle of 100° and an inclination of 50° (Bruderer et al. 2014). The azimuthal profile is extracted at the dust peak radius of 62 au with a radial width of 60 au and the radial profile at the peak ϕ of 192° East-of-North with an azimuthal width of 100°. For ^{13}CO, the data are extracted around the peak radius of 35 au and the peak ϕ of 269°.

The azimuthal profiles show that H_2CO is azimuthally more extended than CH_3OH and is trailing the dust trap, whereas CH_3OH is similar in width as the continuum emission. In contrast, the ^{13}CO emission is present along the entire ring, with a dip around the continuum peak due to continuum oversubtraction (the Band 9 continuum peak is azimuthally shifted w.r.t. to the Band 7 continuum due to different grain sizes traced). The Band 7 line data presented here are only moderately affected by continuum oversubtraction. Radially, the H_2CO profile is cospatial with the continuum emission, although the emission remains radially unresolved. In contrast, the CH_3OH profile appears somewhat further extended outwards and based on the line wings, also inwards. The ^{13}CO emission peaks radially inside the dust continuum peak.

4. Analysis

With multiple line transitions it is possible to derive the column density and excitation temperature for both molecules under the assumption of LTE and optically thin emission (or a correction for optical depth). The optical depth is determined first using the expected emission from the emitting area. As the zero-moment maps of H_2CO and CH_3OH are marginally resolved, the emitting area cannot be reliably determined from these images. In-

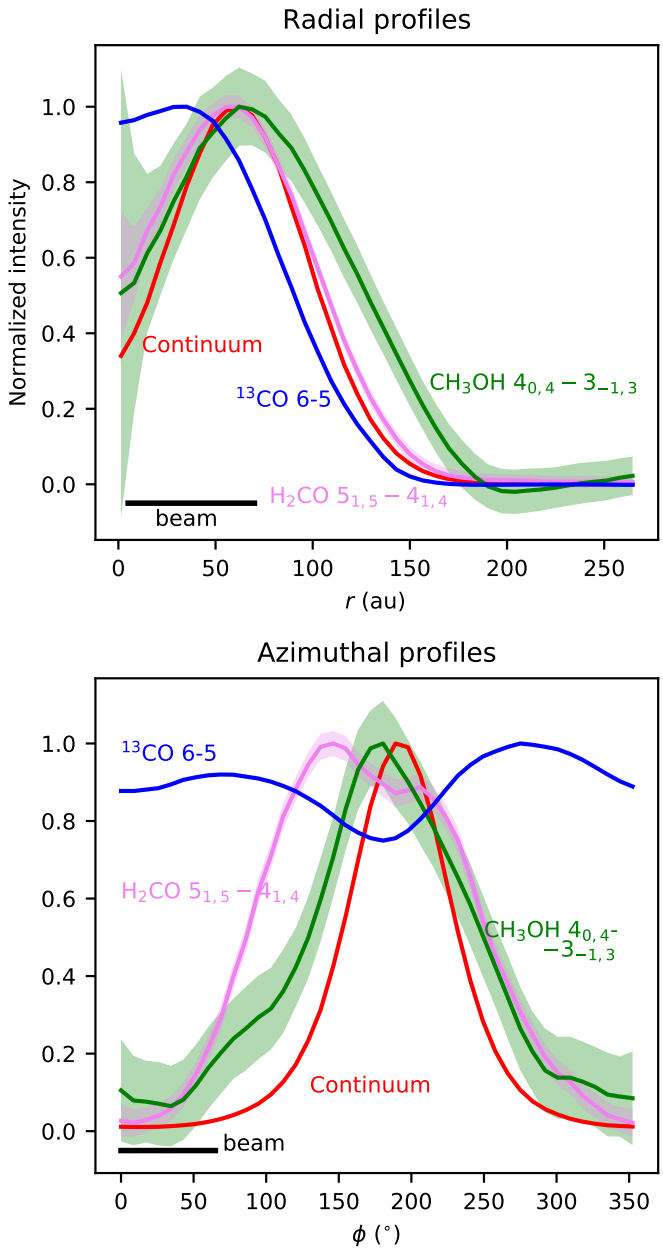

Fig. 2. Radially and azimuthally averaged profiles of the brightest H_2CO and CH_3OH lines from the Briggs weighted images, combined with the profiles from ^{13}CO 6-5 and the 355 GHz continuum imaged at the same beam size of 0.55×0.44".

stead, the emitting area is determined using the high resolution (0.18×0.14") Band 7 continuum image (Francis & van der Marel 2020, and Figure A.3), with the underlying assumption that the H_2CO and CH_3OH emission follow the morphology of the dust crescent. Although the H_2CO emission is azimuthally more extended than the continuum, the difference is marginal (∼20% in the convolved images) and can be ignored. The emitting area of the high-resolution continuum is $1.4{\cdot}10^{-11}$ sr with a 5σ threshold.

Using this emitting area, the optical depth τ and the column densities of individual levels N_u are estimated following the excitation equations in Loomis et al. (2018). All lines are optically thin with $\tau < 0.1$ for $T > 100$ K. The ortho-to-para ratio of H_2CO in the degeneracies and partition functions is taken as 3, and the A/E ratio of CH_3OH as 1. The column density N_T and temperature $T_{\rm rot}$ are estimated by fitting the rotational diagrams using the `emcee` package to compute the posterior distributions (Foreman-Mackey et al. 2013), assuming optically thin emission. Our best-fit results are shown in Figure 3 and indicate an average column density of $7.7{\pm}0.5 \cdot 10^{13}$ cm^{-2} and $4.9{\pm}0.2 \cdot 10^{14}$ cm^{-2}, and a rotational temperature of 173^{+11}_{-9} and 103^{+6}_{-5} K for H_2CO and CH_3OH, respectively (see Figure B.1). This implies that the temperature of H_2CO is higher than CH_3OH and the abundance ratio H_2CO/CH_3OH is 0.16±0.01, much lower than found for other disks (Booth et al. 2021), and suggestive of ice-dominated chemistry. However, it is possible that the transitions trace multiple regimes with different temperatures in the disk. Furthermore, the ortho-to-para ratio obtained by fitting the ortho and para lines separately is <3, which is potentially pointing to an ice formation route as well (Terwisscha van Scheltinga et al. 2021), but could also be caused by optical depth (see Appendix B). The gas surface density derived by van der Marel et al. (2016) at 60 au radius corresponds to $N_{\rm H_2} \sim 1.6 \cdot 10^{22}$ cm^{-2}, so the relative abundances of H_2CO and CH_3OH are $\sim 10^{-8}$ w.r.t. H_2, consistent with previous estimates by van der Marel et al. (2014).

The excitation temperature (rotational temperature) is equal to the kinetic temperature under the assumption of LTE at high densities. H_2CO lines are particularly good diagnostics of kinetic temperature, since radiative transitions are not allowed between the different K_p ladders. The relative populations of those ladders are therefore dominated by collisions only (Mangum & Wootten 1993; van Dishoeck et al. 1993). The LTE assumption and corresponding kinetic temperature can be tested using a calculation of the balance between excitation and de-excitation using RADEX (van der Tak et al. 2007). Collisional rate coefficients are taken from the LAMDA database for the individual molecules (Rabli & Flower 2010; Wiesenfeld & Faure 2013) as summarized in Schöier et al. (2005). We compute line ratios for a range of temperatures and H_2 densities and a molecular column density of 10^{14} cm^{-2} shown in Figure C.3 following van Dishoeck et al. (1995).

The H_2 densities in the midplane and molecular layers of IRS 48 are $\sim 10^{6-8}$ cm^{-3} (Bruderer et al. 2014). In this regime, the line ratios are only sensitive to temperature, with typical inferred values of 200±50 K for H_2CO and 100±20 K for CH_3OH, confirming that the H_2CO emission originates from a warmer layer (Fig. C.3).

5. Discussion and conclusions

The strong detection of CH_3OH and its precursor H_2CO in IRS 48 challenge current chemical disk models, which predict that Herbig disks cannot form COMs in situ due to their warmer midplane (Agúndez et al. 2018). IRS 48 is the second mature Herbig disk with a CH_3OH detection, following HD100546 (Booth et al. 2021). The derived H_2CO/CH_3OH abundance ratio of ∼0.2 in IRS 48 indicates that ice chemistry must be the primary formation mechanism. The warm excitation temperatures >100 K indicates that the emission does not originate from the disk midplane which has a temperature of ∼70 K at 60 au (Bruderer et al. 2014). The continuum brightness temperature at 355 GHz is 27 K, providing a lower limit. H_2CO may originate from slightly higher layers than CH_3OH considering its rotational temperature.

An important clue for the origin of the COM chemistry in IRS 48 is the striking crescent morphology of the emission, which is following the shape of the dust continuum. The asymmetric dust continuum has been interpreted as a dust trap, based

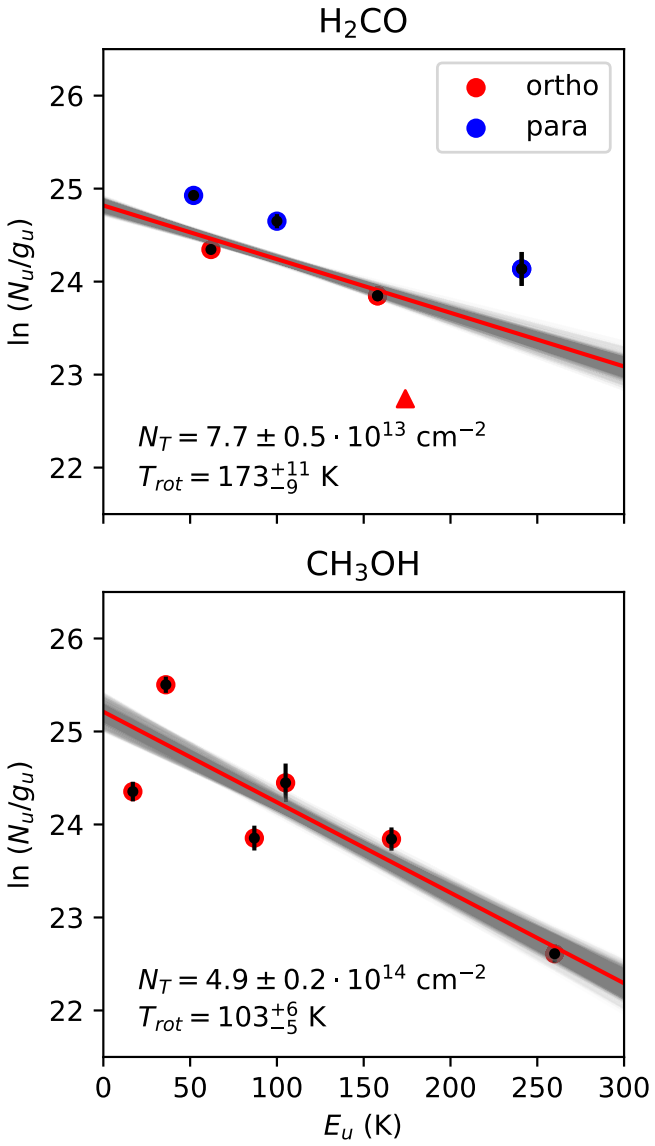

Fig. 3. Rotational diagrams of H_2CO and CH_3OH using the integrated fluxes from this study, assuming optically thin emission. The integrated flux of the H_2CO $9_{1,8}$-$8_{1,7}$ transition from van der Marel et al. (2014) is included as a lower limit. The red line provides the best fit through the data points and the grey lines are draws from the posterior distribution from the fitting (Figure B.1).

on the comparison between large grains, small grains and gas (van der Marel et al. 2013). The high degree of chemical complexity may thus be related to special physical conditions there. Large grains concentrate in a dust trap and grow efficiently to larger sizes due to the higher dust concentration and lower destructive collision efficiency (Weidenschilling 1977; Brauer et al. 2008; Pinilla et al. 2012b). Small grains are still continuously produced by fragmentation. The dust trap thus provides a large reservoir of icy dust grains, and if these have been either radially transported from the outer part of the disk or inherited from the early, colder stages they might be rich in ices (Krijt et al. 2020; Booth et al. 2021). The dust trap thus acts as an 'ice trap' of large icy dust grains, as previously suggested for TW Hya (Walsh et al. 2016). Considering typical interstellar ice abundances of CH_3OH of $3 \cdot 10^{-6}$ (Boogert et al. 2015) and model COM ice abundances in the disk midplane of $\geq 10^{-6}$ (Walsh et al. 2014), only a fraction of the ice content is sublimated.

The dust density distribution in the dust trap plays a crucial role here, as dust grains limit the UV field penetration in the disk, lowering the dust and gas temperature (Bruderer et al. 2012). Ohashi et al. (2020) derived a dust surface density as high as 2-8 g cm^{-2} at the dust trap radius based on polarization continuum measurements and constraints from the centimeter emission in IRS 48. This is well above the gas surface density of 0.07 g cm^{-2} derived from CO isotopologues and DALI modelling by van der Marel et al. (2016), implying a dust-to-gas ratio $\gg$1. Using a series of physical-chemical models with different dust surface densities, we estimate the temperature in the disk at the location of the dust trap. Two sets of models are run: first, only the dust density of the large grains in the midplane is increased (settled models) and second, the dust density is increased throughout the column (full models). The details of the vertical and radial structure of gas and dust of the models are described in Appendix C.

Figure 4 shows the midplane temperature profiles and the vertical gas temperature profiles at 65 au (away from the edge), based on the model output (Figure C.1-C.2). The gas temperature is coupled to the dust temperature in the midplane, up to $z/r \lesssim 0.15$. Figure 4 demonstrates that the midplane temperature may get as low as 40 K in the dust trap, well below the H_2CO sublimation temperature of 66 K (Penteado et al. 2017). The temperature is unlikely to be below the CO freezeout temperature of 22 K, so continuous formation of H_2CO and CH_3OH through CO ice hydrogenation is not possible. However, the dust trap contains a very large reservoir of icy grains. In order to sublimate, icy grains containing H_2CO and CH_3OH need to be vertically transported to the higher, warmer layers in the disk. The right panel in Figure 4 shows that the temperature reaches >100 K at a height of z/r ~0.2 for the settled models, in the emitting layer of H_2CO and CH_3OH. The full models reach temperature of only 80 K, not high enough to explain the observed excitation temperatures, suggesting that the high dust concentration of large dust grains must be settled to the midplane. We note that the gas temperature in the warm molecular layer in IRS48 is estimated as 250-350 K from mid-J rotational CO lines (Fedele et al. 2016), and also that the brightness temperature of the ^{13}CO 6–5 line is as high as ~200 K (van der Marel et al. 2016).

This distribution of icy dust grains and molecules requires efficient vertical transport in the disk which can be achieved by turbulent mixing (Semenov & Wiebe 2011). In addition, the dynamics of the vortex itself may play a role, as both the vertical shear instability (Flock et al. 2020) and meridional flows (Meheut et al. 2010) in vortices increase the vertical mixing. The full scenario of the ice reservoir, mixing and sublimation is summarized in the bottom panels of Figure 4.

The morphology of the COM emission suggests that the combination of a concentration of icy dust pebbles and the irradiation of the cavity wall (resulting in a thin layer of thermal sublimation as proposed by Cleeves et al. 2011) increase the chemical complexity in IRS 48. It is also important to point out that the COM emission is unlikely to trace an actual azimuthal gas overdensity in the disk: considering the high SNR, the azimuthal contrast would have to be more than a factor of 10, and such a contrast was not detected in the $C^{18}O$ 6-5 isotopologue emission (van der Marel et al. 2016), which is optically thin considering the ratio of 4.3±1.4 with the $C^{17}O$ flux measured by Bruderer et al. (2014).

The difference in azimuthal extent between H_2CO and CH_3OH could be explained by the lower desorption tempera-

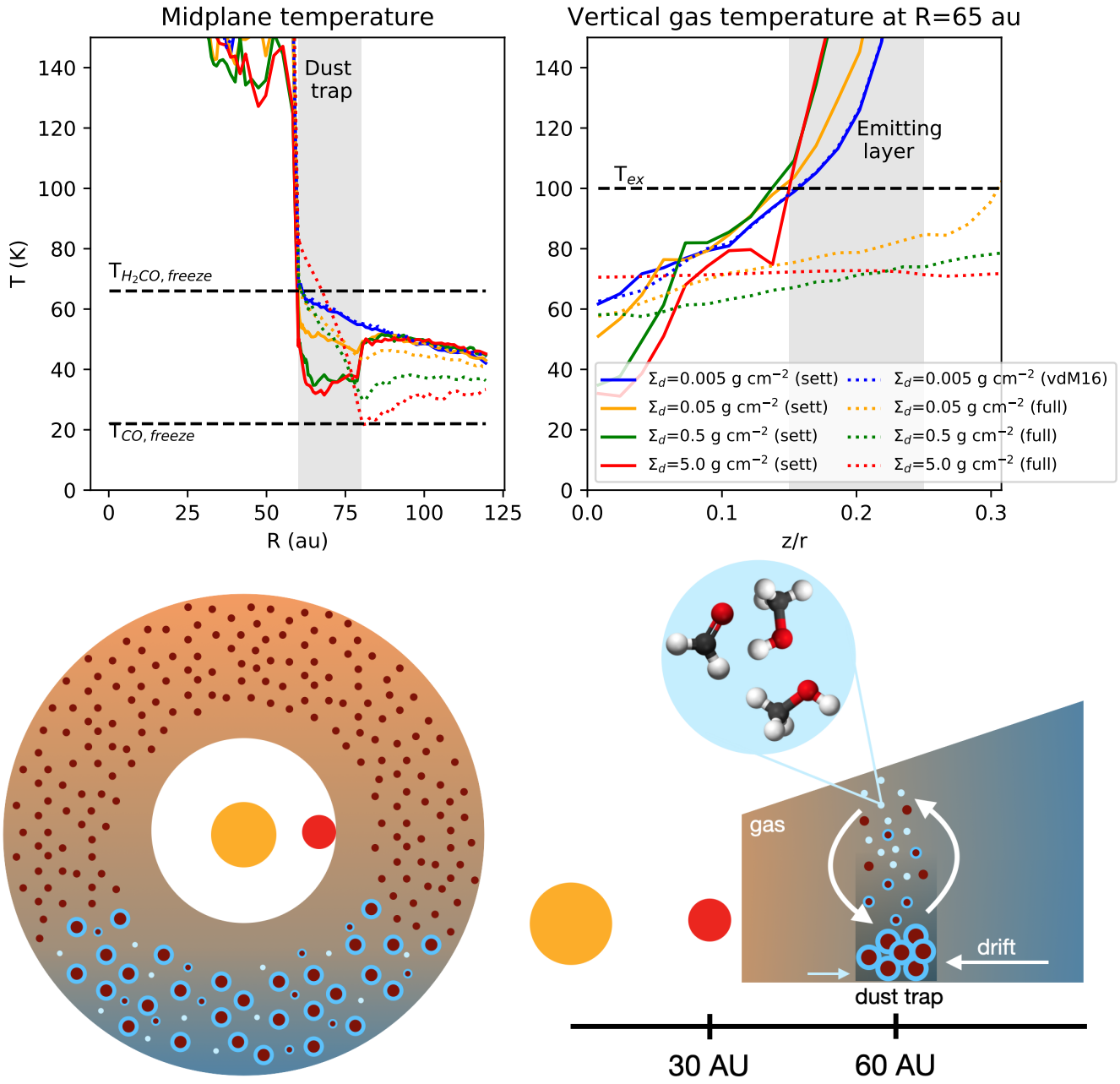

Fig. 4. Top left: Radial dust temperature profiles of the midplane. **Top right:** Vertical gas temperature profiles at 65 au, just inside the dust trap. Both temperature profiles are based on our physical-chemical DALI models with different dust surface densities (Figure C.1,C.2). In the midplane, the gas temperature is equal to the dust temperature. The plots demonstrate that the dust trap provides sufficiently low temperatures for a COM ice reservoir in the settled midplane, whereas the temperatures in the emitting layer are sufficiently high to explain the derived excitation temperatures. **Bottom:** Sketch of the proposed scenario for the complex organic chemistry in a dust trap based on this work. The blue-orange gradient indicates the predicted temperature structure in the disk the large arrows the vertical and radial transport of the icy pebbles, and the small arrow the thermal desorption at the inner edge of the dust trap

.

ture of H_2CO compared to CH_3OH. This discrepancy cannot be explained by additional gas phase chemistry production, as this would result in H_2CO emission along the entire ring. Formation by gas phase chemistry is not excluded but due to the extreme dust trapping the ice sublimation dominates the observable chemistry.

It is unclear whether the high dust-to-gas ratio environment and high COM abundances are unique for IRS 48. Pegues et al. (2020) and Facchini et al. (2021) derive H_2CO column densities of $\sim 10^{12}$ cm^{-2} and low excitation temperatures of 20-30 K for a number of T Tauri disks, whereas for HD100546, the rotational temperature in the inner 50 au was derived as 50-100 K (Booth et al. 2021). All these T Tauri disks have radial dust traps, which also lead to dust concentrations smaller than the beam size of the COM observations. Interestingly, Pegues et al. (2020) find a higher column density of $\sim 10^{13}$ cm^{-2} for J1604-2130, the only disk in their sample for which the H_2CO emission is more resolved radially, revealing the ring structure also seen

in the continuum. As the inferred column densities rely on the assumed emitting area, the column densities in these works are lower limits and may be as high as in IRS 48. However, the high excitation temperatures of the COMs in IRS 48 require more efficient vertical transport, which may be due to the unique vortex properties.

IRS 48 is the first protoplanetary disk with a clear link between the morphology of the COM emission and the continuum. These results show the importance of taking into account dust traps in chemical disk models in the production of complex organic chemistry, and in spatially resolving COMs in disks for comparison with the dust substructure.

Acknowledgements. We thank the referee for their thoughtful report, which has improved the clarity of the manuscript. We would also like to thank Wlad Lyra and Sebastiaan Krijt for useful discussions and Akimasa Kataoka for his help with the reduction of the data. N.M. acknowledges support from the Banting Postdoctoral Fellowships program, administered by the Government of Canada. ALMA is a partnership of ESO (representing its member states), NSF (USA) and NINS (Japan), together with NRC (Canada) and NSC and ASIAA (Taiwan) and KASI (Republic of Korea), in cooperation with the Republic of Chile. The Joint ALMA Observatory is operated by ESO, AUI/ NRAO and NAOJ. This paper makes use of the following ALMA data: 2017.1.00834.S.

References

Agúndez, M., Roueff, E., Le Petit, F., & Le Bourlot, J. 2018, A&A, 616, A19
Alarcón, F., Teague, R., Zhang, K., Bergin, E. A., & Barraza-Alfaro, M. 2020, ApJ, 905, 68
Andrews, S. M., Huang, J., Pérez, L. M., et al. 2018, ApJ, 869, L41
Andrews, S. M., Wilner, D. J., Espaillat, C., et al. 2011, ApJ, 732, 42
Barge, P. & Sommeria, J. 1995, A&A, 295, L1
Bergin, E. A., Aikawa, Y., Blake, G. A., & van Dishoeck, E. F. 2007, Protostars and Planets V, 751
Boogert, A. C. A., Gerakines, P. A., & Whittet, D. C. B. 2015, ARA&A, 53, 541
Booth, A. S., Walsh, C., Terwisscha van Scheltinga, J., et al. 2021, Nature Astronomy [arXiv:2104.08348]
Brauer, F., Dullemond, C. P., & Henning, T. 2008, A&A, 480, 859
Bruderer, S. 2013, A&A, 559, A46
Bruderer, S., van der Marel, N., van Dishoeck, E. F., & van Kempen, T. A. 2014, A&A, 562, A26
Bruderer, S., van Dishoeck, E. F., Doty, S. D., & Herczeg, G. J. 2012, A&A, 541, A91
Cleeves, L. I., Bergin, E. A., Bethell, T. J., et al. 2011, ApJ, 743, L2
Cridland, A. J., Pudritz, R. E., & Birnstiel, T. 2017, MNRAS, 465, 3865
Dutrey, A., Guilloteau, S., & Guelin, M. 1997, A&A, 317, L55
Ehrenfreund, P. & Charnley, S. B. 2000, ARA&A, 38, 427
Facchini, S., Teague, R., Bae, J., et al. 2021, arXiv e-prints, arXiv:2101.08369
Fedele, D., van Dishoeck, E. F., Kama, M., Bruderer, S., & Hogerheijde, M. R. 2016, A&A, 591, A95
Flock, M., Turner, N. J., Nelson, R. P., et al. 2020, ApJ, 897, 155
Foreman-Mackey, D., Hogg, D. W., Lang, D., & Goodman, J. 2013, PASP, 125, 306
Francis, L. & van der Marel, N. 2020, ApJ, 892, 111
Fuchs, G. W., Cuppen, H. M., Ioppolo, S., et al. 2009, A&A, 505, 629
Gaia Collaboration, Brown, A. G. A., Vallenari, A., et al. 2018, A&A, 616, A1
Garrod, R., Park, I. H., Caselli, P., & Herbst, E. 2006, Faraday Discussions, 133, 51
Geers, V. C., Pontoppidan, K. M., van Dishoeck, E. F., et al. 2007, A&A, 469, L35
Hama, T., Kouchi, A., & Watanabe, N. 2018, ApJ, 857, L13
Herbst, E. & van Dishoeck, E. F. 2009, ARA&A, 47, 427
Kahane, C., Frerking, M. A., Langer, W. D., Encrenas, P., & Lucas, R. 1984, A&A, 137, 211
Krijt, S., Bosman, A. D., Zhang, K., et al. 2020, ApJ, 899, 134
Lee, J.-E., Lee, S., Baek, G., et al. 2019, Nature Astronomy, 3, 314
Loomis, R. A., Öberg, K. I., Andrews, S. M., et al. 2018, AJ, 155, 182
Mangum, J. G. & Wootten, A. 1993, ApJS, 89, 123
Meheut, H., Casse, F., Varniere, P., & Tagger, M. 2010, A&A, 516, A31
Mulders, G. D., Waters, L. B. F. M., Dominik, C., et al. 2011, A&A, 531, A93
Öberg, K. I. & Bergin, E. A. 2021, Phys. Rep., 893, 1
Öberg, K. I., Guzmán, V. V., Furuya, K., et al. 2015, Nature, 520, 198
Öberg, K. I., Qi, C., Fogel, J. K. J., et al. 2010, ApJ, 720, 480
Ohashi, S., Kataoka, A., van der Marel, N., et al. 2020, ApJ, 900, 81
Pegues, J., Öberg, K. I., Bergner, J. B., et al. 2020, ApJ, 890, 142
Penteado, E. M., Walsh, C., & Cuppen, H. M. 2017, ApJ, 844, 71
Pérez, L. M., Isella, A., Carpenter, J. M., & Chandler, C. J. 2014, ApJ, 783, L13
Pinilla, P., Benisty, M., & Birnstiel, T. 2012a, A&A, 545, A81
Pinilla, P., Birnstiel, T., Ricci, L., et al. 2012b, A&A, 538, A114
Podio, L., Garufi, A., Codella, C., et al. 2020, A&A, 642, L7
Rabli, D. & Flower, D. R. 2010, MNRAS, 406, 95
Schöier, F. L., van der Tak, F. F. S., van Dishoeck, E. F., & Black, J. H. 2005, A&A, 432, 369
Semenov, D. & Wiebe, D. 2011, ApJS, 196, 25
Terwisscha van Scheltinga, J., Hogerheijde, M. R., Cleeves, L. I., et al. 2021, ApJ, 906, 111
Thi, W.-F., van Zadelhoff, G.-J., & van Dishoeck, E. F. 2004, A&A, 425, 955
van der Marel, N., Pinilla, P., Tobin, J., et al. 2015, ApJ, 810, L7
van der Marel, N., van Dishoeck, E. F., Bruderer, S., et al. 2016, A&A, 585, A58
van der Marel, N., van Dishoeck, E. F., Bruderer, S., et al. 2013, Science, 340, 1199
van der Marel, N., van Dishoeck, E. F., Bruderer, S., & van Kempen, T. A. 2014, A&A, 563, A113
van der Tak, F. F. S., Black, J. H., Schöier, F. L., Jansen, D. J., & van Dishoeck, E. F. 2007, A&A, 468, 627
van Dishoeck, E. F., Blake, G. A., Draine, B. T., & Lunine, J. I. 1993, in Protostars and Planets III, ed. E. H. Levy & J. I. Lunine, 163
van Dishoeck, E. F., Blake, G. A., Jansen, D. J., & Groesbeck, T. D. 1995, ApJ, 447, 760
van 't Hoff, M. L. R., Tobin, J. J., Trapman, L., et al. 2018, ApJ, 864, L23
Walsh, C., Juhász, A., Meeus, G., et al. 2016, ApJ, 831, 200
Walsh, C., Millar, T. J., Nomura, H., et al. 2014, A&A, 563, A33
Watanabe, N. & Kouchi, A. 2002, ApJ, 571, L173
Weidenschilling, S. J. 1977, MNRAS, 180, 57
Wiesenfeld, L. & Faure, A. 2013, MNRAS, 432, 2573

Appendix A: Spectra and intensity maps

This section contains additional figures of the data.

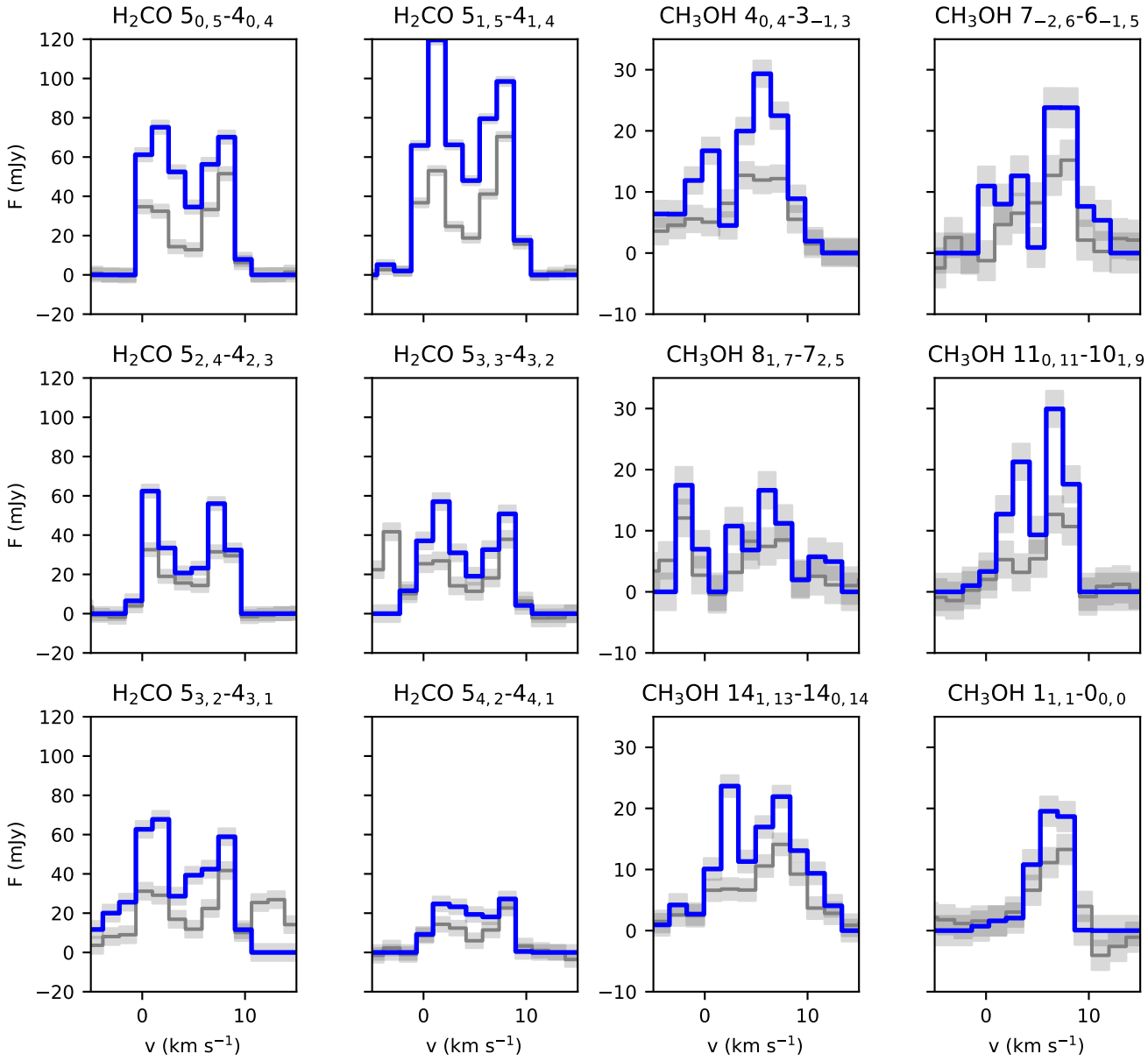

Fig. A.1. H_2CO and CH_3OH spectra, integrated over the central area of the dust trap using Keplerian masking (blue) and extracted from a rectangular box (grey). The grey shades indicate the noise levels in the spectra. The spectra are ordered by increasing E_u, following the values reported in Table 1.

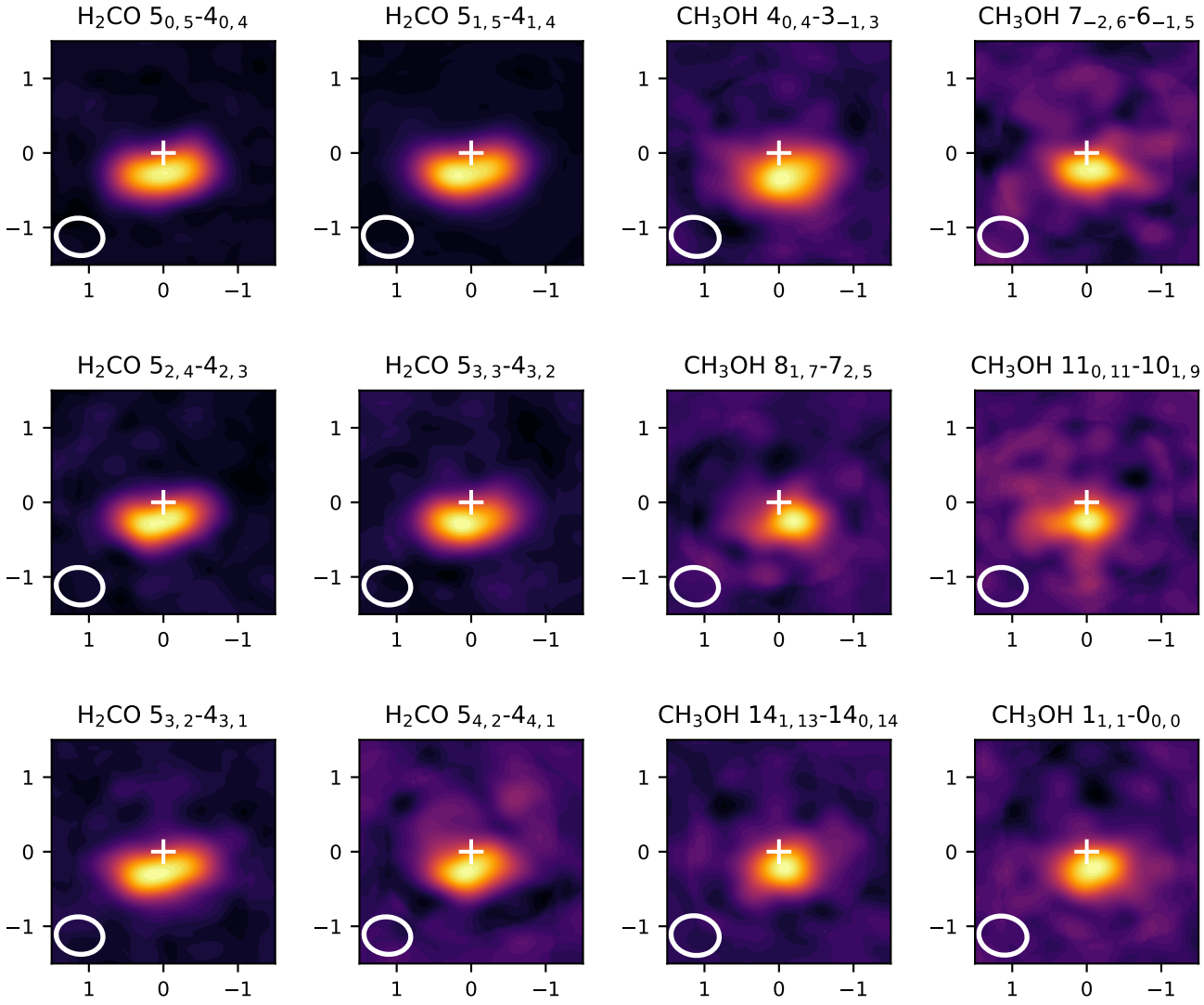

Fig. A.2. H_2CO and CH_3OH naturally weighted zero moment maps using Keplerian masking. The plus indicates the position of the star and the beam is shown in the lower left of each map.

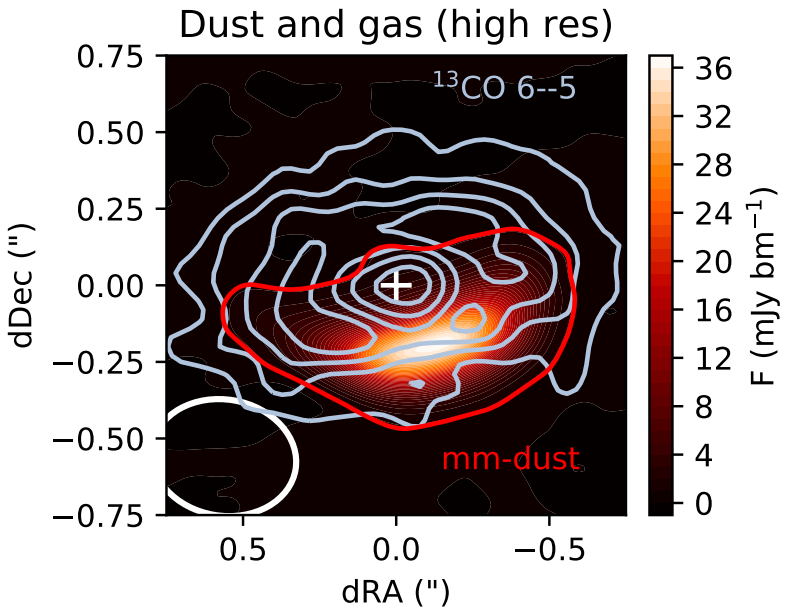

Fig. A.3. High resolution image of the ^{13}CO 6–5 zero moment map (blue) and the 366 GHz continuum (red) at the original 0.18×0.14" resolution. The contours of the ^{13}CO show the 20,40,60,80% of the peak while the contours of the continuum indicate the 5σ level. This image demonstrates that the gas traces a full disk ring whereas the mm-dust grains are concentrated in the southern part of the disk.

Appendix B: Rotational diagram analysis

This section contains more details on the analysis of the rotational diagram from Figure 3. Figure B.1 shows the corner plots showing the posterior distributions and covariances of the fit containing all line transitions, confirming the fit has converged. The covariance is similar to previous studies of rotational diagrams of COMs in protoplanetary disks (e.g. Loomis et al. 2018).

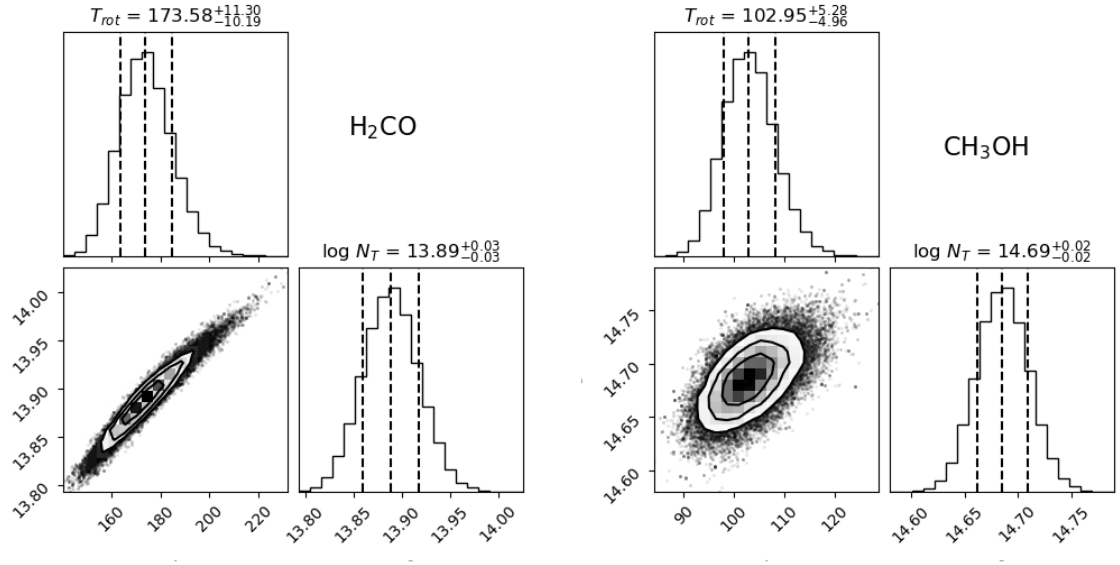

Fig. B.1. Posterior distributions of the column density and rotational temperature based on our optically thin line intensities of H_2CO (left) and CH_3OH (right). The best fit is shown in Figure 3.

Second, we estimate the ortho-to-para ratio of H_2CO by fitting the ortho and para lines separately, without the ortho-to-para correction of 3 in the degeneracies as used in Figure 3. The new rotational diagram with best fits and the posteriors are shown in Figure B.2. The ortho lines have a best fit $T_{\rm rot}$ of 193^{+18}_{-15} K and $N_T = 7.2 \pm 0.7 \cdot 10^{13}$ cm^{-2} and the para lines a $T_{\rm rot}$ of 257^{+57}_{-39} K and $N_T = 5.9 \pm 1.7 \cdot 10^{13}$ cm^{-2}. This implies an ortho-to-para ratio of 1.2±0.4, which is well below the default value of 3. The lower value could indicate an ice formation rather than gas formation route (e.g Terwisscha van Scheltinga et al. 2021), which is consistent with our proposed scenario. However, if the optical depth of the ortho lines is underestimated (if the emitting area is smaller than assumed) this could also explain the lower value. Furthermore, for H_2O it has been shown that the ortho-to-para ratio is reset after desorption from the ices (Hama et al. 2018) and if the same is true for H_2CO, the ortho-to-para ratio does not provide information

about the formation origin. Regardless of the precise scenario, a low ortho-to-para ratio would imply a very cold formation location of only ~10 K (Kahane et al. 1984), much lower than the current dust trap conditions.

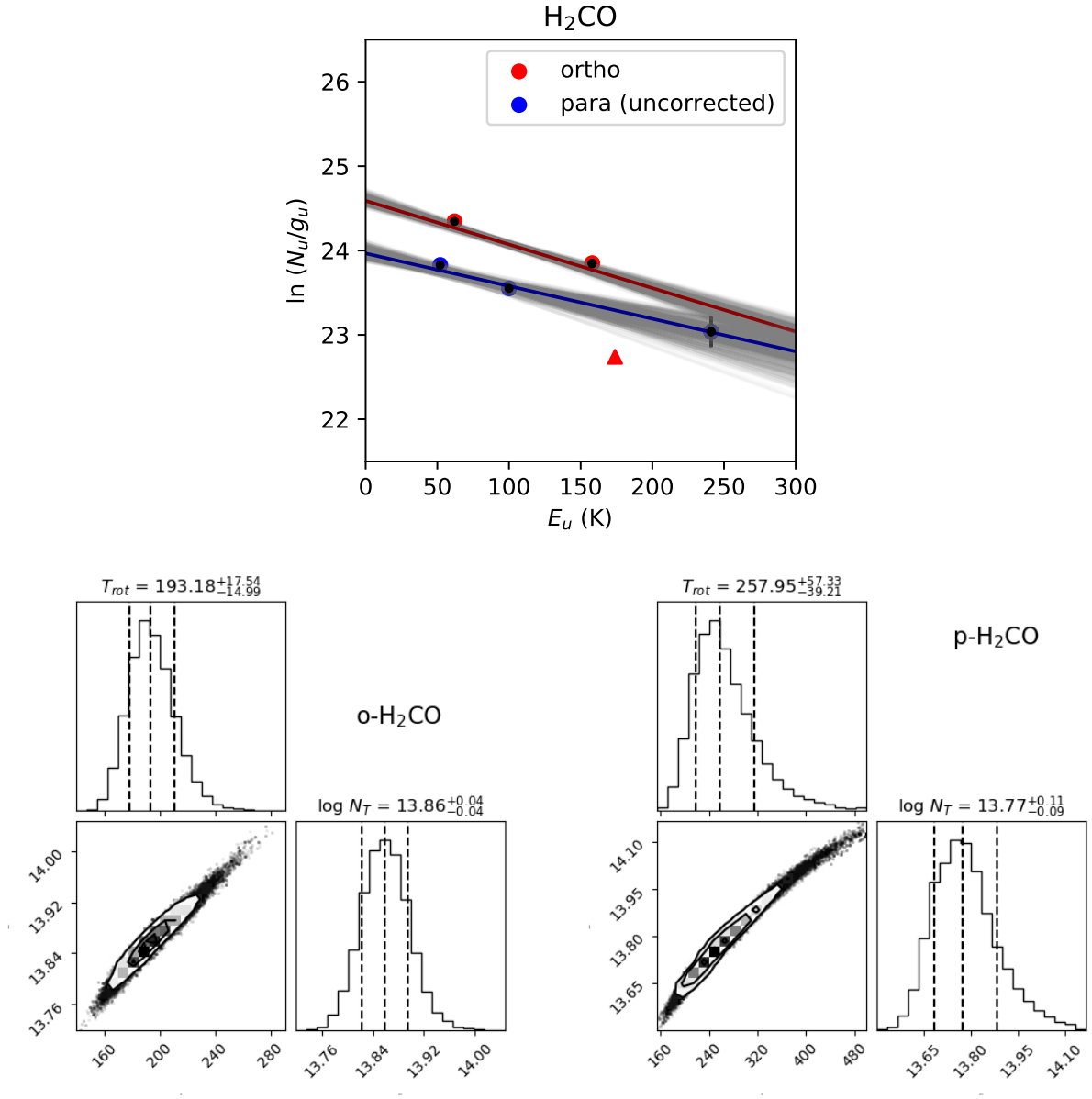

Fig. B.2. Rotational diagram of H_2CO, similar to Figure 3, but without the default ortho-to-para correction of 3 for the para lines, with separate fits to the ortho and para lines. The bottom panels show the posterior distributions of the best fits as in Figure B.1.

Appendix C: Temperature structure

This section describes our analysis of the temperature structure and line ratios of IRS 48. We set up a series of physical-chemical models using DALI (Bruderer et al. 2012; Bruderer 2013) to compute the gas and dust temperature structure from the heating-cooling balance of gas and dust, following the parametrized model of the gas and dust surface density from van der Marel et al. (2016) that is consistent with the CO 6–5 isotopologue data presented in that work. The dust surface density was not explicitly fit in that model, and with a gas-to-dust ratio of 20 used in that work the dust surface density at 60 au is Σ_d ~0.005 g cm^{-2}. As Ohashi et al. (2020) derived a much higher dust surface density of Σ_d ~2-8 g cm^{-2}, we explore the effect of the dust surface density on the radial and vertical temperature structure, using Σ_d ~0.05, 0.5 and 5.0 g cm^{-2} between 60 and 80 au. Two sets of models are run: one with an increase of the large grains in the midplane with a larger degree of settling (settled models) and second with an increase of all grains throughout the full dust column (full models). The vertical density structure in DALI is fixed to a Gaussian profile with different scale heights for the large and small grains to represent the settling, following Andrews et al. (2011):

$$\rho_l = \frac{\Sigma_l}{\sqrt{2\pi} r \chi h} \exp\left[-\frac{1}{2}\left(\frac{\pi/2-\theta}{\chi h}\right)^2\right] \quad \text{(C.1)}$$

$$\rho_s = \frac{\Sigma_s}{\sqrt{2\pi} r h} \exp\left[-\frac{1}{2}\left(\frac{\pi/2-\theta}{h}\right)^2\right] \quad \text{(C.2)}$$

with ρ_l and ρ_s the dust density of large and small grains, respectively, $h = h_c(r/r_c)^{\psi}$ the scale height, χ the settling parameter and θ the vertical latitude coordinate measured from the pole. The large grain population contains dust grains from 0.005 μm to 1 mm and the small grain population contains dust grains from 0.005 - 1 μm by convention. In the full disk model, the settling degree χ is set to the default value of 0.2, while in the settled model χ is set to 0.1. The radial structure inside 60 au contains the inner dust disk (between $r_{\rm sub}$ and $r_{\rm gap}$), the gas cavity $r_{\rm cavgas}$ and dust cavity $r_{\rm cavdust}$, which are the same as in van der Marel et al. (2016) and we refer for more details to that work. All model parameter values are listed in Table C.1 and the results are shown in Figure C.1 and C.2.

Table C.1. Model parameters of gas and dust surface density

Property	Parameter	Settled models	Full models
Surface density	$\Sigma_{\rm 60au,gas}$ (g cm^{-2})	0.25	0.25
	$\Sigma_{\rm 60au,dust}$ (g cm^{-2})	0.005,0.05,0.5,5.0 (large grains only)	0.005,0.05,0.5,5.0 (all grains)
Dust settling	χ	0.1	0.2
Vertical structure	h_c	0.14	0.14
	ψ	0.22	0.22
Radial structure	r_c (au)	60	60
	$r_{\rm sub}$ (au)	0.4	0.4
	$r_{\rm gap}$ (au)	1	1
	$r_{\rm cavgas}$ (au)	25	25
	$r_{\rm cavdust}$ (au)	60	60
	$r_{\rm out}$ (au)	90	90

Second, we estimate the expected flux ratios for both optically thick and optically thin emission of the H_2CO and CH_3OH lines studied in this work. This is parametrized by setting an abundance of 10^{-7} and 10^{-9} (optically thick and thin, respectively) for both molecules in the regions in the disk where the extinction A_V >1 (shielding for photodissociation), radius r >60 au (in the dust trap) and the dust temperature $T_{\rm dust} > T_{\rm subl}$, with $T_{\rm subl}$=66 K for H_2CO and 100 K for CH_3OH. These thresholds set the region where the molecule is expected to be in the gas phase. These regions are well above the regime where the majority of the large grains are located due to the settling. In the rest of the disk, these molecular abundances are set to 10^{-12}. This leads to specific emitting layers in the disk where H_2CO and CH_3OH are located, which are used to raytrace the lines to compute line ratios which can be compared with the data. The absolute fluxes are less relevant as the real molecular layers are likely much more complex. Also, as DALI is an axisymmetric model, the azimuthal structure is not constrained in this model.

The models show that the dust and gas temperature drop when the dust density is increased due to the stronger suppression of the UV field. This drop remains limited to the midplane when the dust density is only increased in that region compared to an increase throughout the full column. This is illustrated directly in Figure 4. The models show that the emitting layer shifts upward in the disk for higher dust densities when the dust is distributed throughout the disk ('full') due to the sublimation temperature requirement. On the upper end, the emitting layer is constrained by the extinction requirement, which means that the layer becomes thinner in the high dust density models. In the most extreme case of Σ_d=5 g cm^{-2} an additional emitting layer appears in the midplane as the dust becomes fully optically thick at the dust edge, leading to a strong vertical increase in temperature.

The raytraced line fluxes reproduce the H_2CO fluxes reasonably well for the settled models for the 10^{-7} abundance, the CH_3OH fluxes are at least a factor 10 too low. The models with 10^{-9} abundance and high dust density full models underestimate all fluxes by 1 to 3 orders of magnitude. The line ratios are derived and compared with the line ratios in the RADEX plot in Figure C.3. The line ratios for H_2CO for 10^{-7} abundance are closer to the data values, suggesting that the H_2CO emission is potentially optically thick (i.e. the emitting area is at least a factor 5 smaller than our estimate). The ratios shift to slightly lower values for the higher dust density models, consistent with lower temperatures. For CH_3OH the ratios are essentially the same for the two abundances and in similar temperature regime as the data, suggesting the emission remains optically thin for both. The ratios shift to higher values for the high dust density full models, consistent with higher temperatures, which is the result of the strong upward shift in the emitting layers. However, the column density and flux drop significantly in that case, implying that this is not a realistic scenario. Overall, the spread in temperatures for the different ratios implies that the various lines trace different temperature regions in the disk with potentially different abundances. A more detailed analysis is saved for future work.

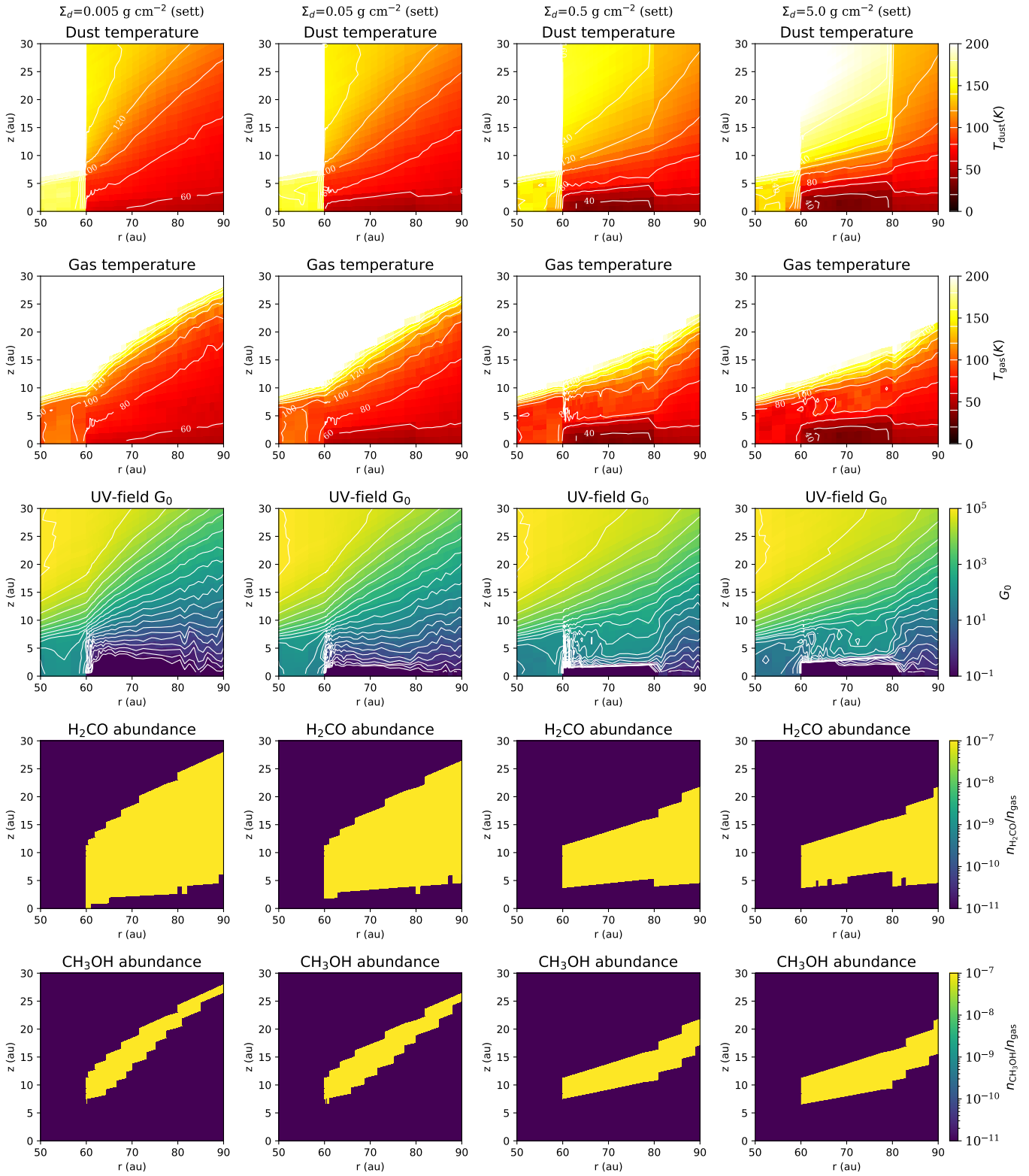

Fig. C.1. Temperature structure of the IRS 48 disk as computed by DALI, using the gas and dust density profile derived by van der Marel et al. (2016) for the settled models (dust density increase of the large grains in the midplane)
. The columns show the influence of the assumed dust surface density (or dust-to-gas ratio, as the gas surface density is set constant) on the UV field and gas temperature. The white contours in the temperature plots indicate steps of 20 K.

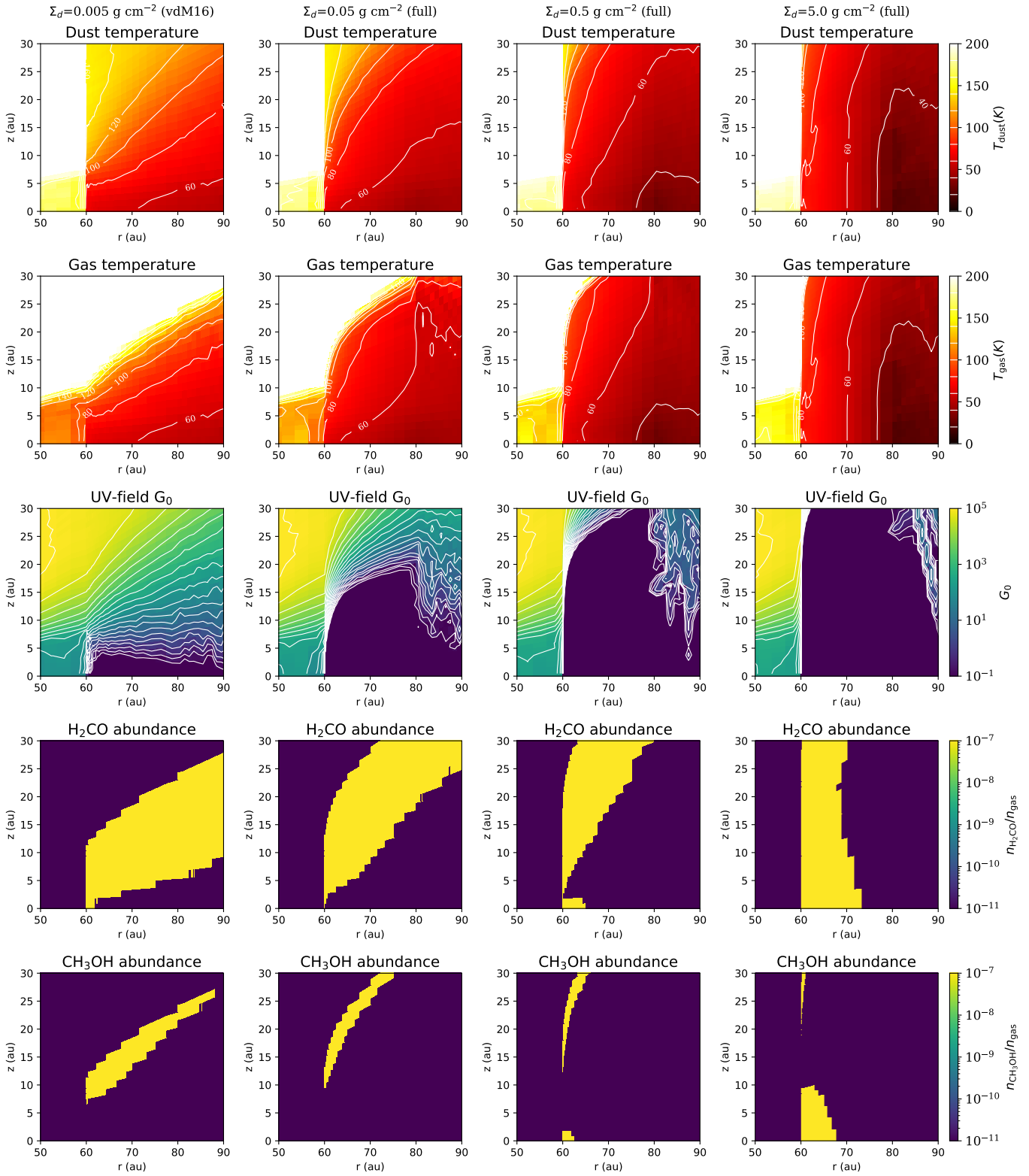

Fig. C.2. Temperature structure of the IRS 48 disk as computed by DALI, using the gas and dust density profile derived by van der Marel et al. (2016) for the full models (dust increase across the column). The columns show the influence of the assumed dust surface density (or dust-to-gas ratio, as the gas surface density is set constant) on the UV field and gas temperature. The white contours in the temperature plots indicate steps of 20 K.

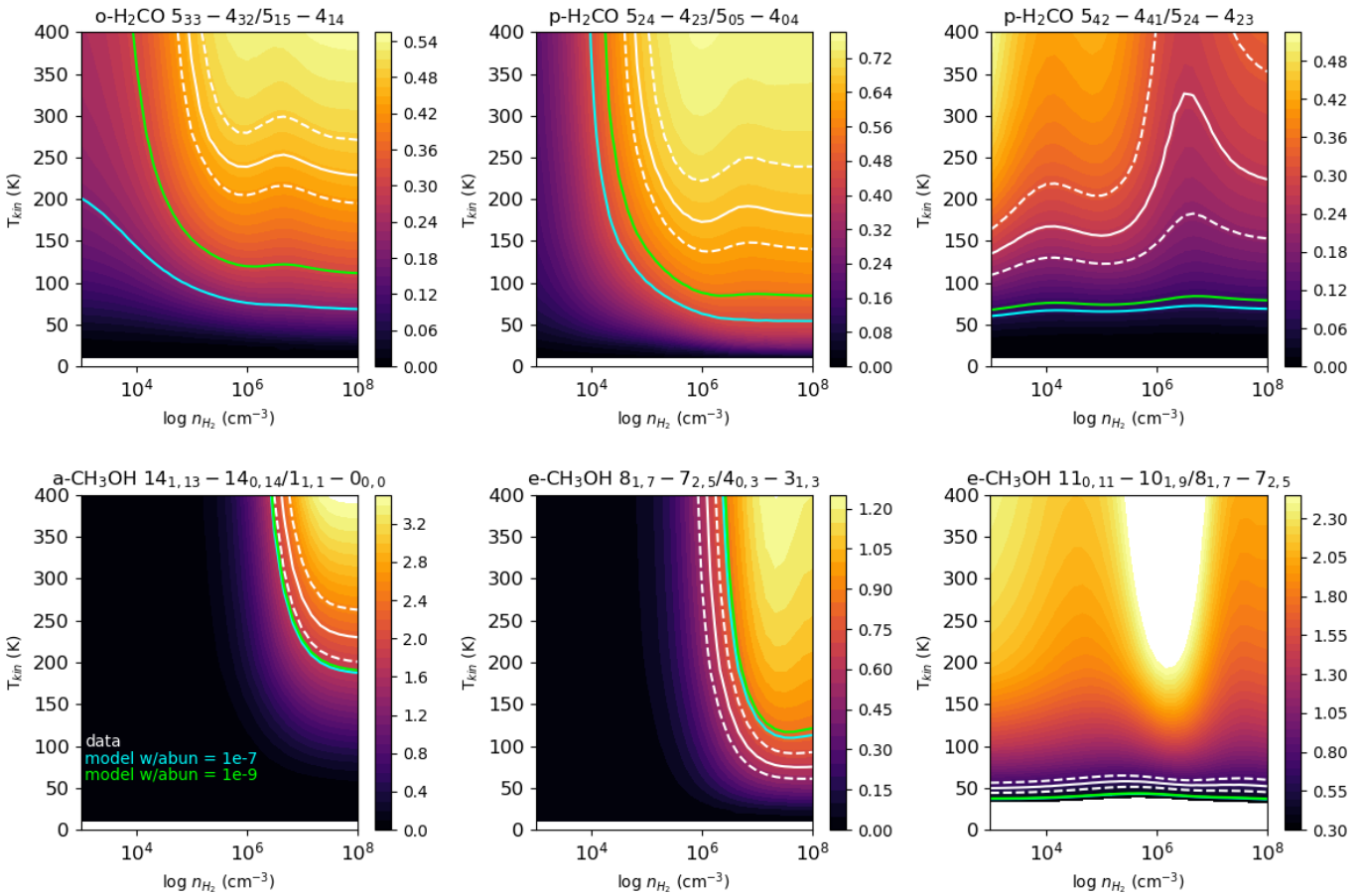

Fig. C.3. Expected line ratios as computed by RADEX for H_2CO (top) and CH_3OH (bottom) for a column density of 10^{14} cm^{-2}. The white contours indicate the observed values and the dashed lines the uncertainty. The coloured lines indicate the ratios as computed for our DALI models of the settled model for fixed abundances 10^{-7} and 10^{-9} in specific emitting layers as described in the text.